Synthesis, Characterization, and Stability of Two Americium Vanadates, $AmVO_3$ and $AmVO_4$

Jean-François Vigier,* Thierry Wiss, Natalia Palina, Tonya Vitova, Jean-Yves Colle, Daniel Bouëxière, Daniel Freis, Rudy J. M. Konings, and Karin Popa*

Read Online

ACCESS | ⬛ Metrics & More | 🔲 Article Recommendations | 🆂🅸 Supporting Information

ABSTRACT: In search for chemically stable americium compounds with high power densities for radioisotope sources for space applications, $AmVO_3$ and $AmVO_4$ were prepared by a solid-state reaction. We present here their crystal structure at room temperature solved by powder X-ray diffraction combined with Rietveld refinement. Their thermal and self-irradiation stabilities have been studied. The oxidation states of americium were confirmed by the Am M_5 edge high-resolution X-ray absorption near-edge structure (HR-XANES) technique. Such ceramics are investigated as potential power sources for space applications like radioisotope thermoelectric generators, and they have to endure

extreme conditions including vacuum, high or low temperatures, and internal irradiation. Thus, their stability under self-irradiation and heat treatment in inert and oxidizing atmospheres was tested and discussed relative to other compounds with a high content of americium.
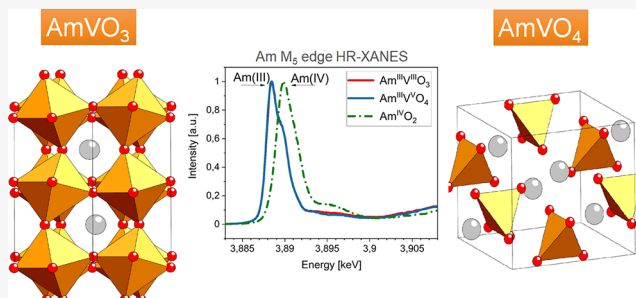
1. INTRODUCTION

The americium isotope ^{241}Am is formed during storage of plutonium via β^--decay of ^{241}Pu with a half-life of 14.33 years. Due to ^{241}Am accumulation in existing stocks of civil-separated plutonium in Europe, and its relatively high specific power of 0.114 W/g, ^{241}Am has been proposed for use in radioisotope power systems (RPSs)[1] and is under consideration by the European Space Agency (ESA) as an energy source for future European space missions.[2] The requirements for a stable solid form are very diverse, ranging from storage on earth and operation in space to safe performance in case of accidents and post-accident scenarios. Our group studied several ceramic forms containing significant specific Am amounts,[3−5] the present study being in line with the past efforts.

The synthesis and crystal structure of $AmVO_3$ were reported for the first time by Keller and co-workers.[6,7] In their work, $AmVO_4$ was prepared by dissolving AmO_2 and V_2O_3 as hydroxides, mixed, dried, and reacted at 1250 °C under an oxidizing atmosphere. The produced $AmVO_4$ was subsequently reduced to obtain $AmVO_3$. The authors proposed the crystal structure for the two compounds (perovskite-type for $AmVO_3$ and zircon-like for $AmVO_4$) and gave the lattice parameters.

According to the Inorganic Crystal Structure Database (ICSD), there are no compounds of americium and vanadium with a fully characterized crystal structure. We present here the complete crystal structure refinement of the two vanadates by Rietveld analysis at room temperature. Spectroscopic and

microscopic studies were carried out to check the purity of the samples. The high-resolution X-ray absorption near-edge structure (HR-XANES) technique was applied at the Am M_5 edge to characterize the Am oxidation states. The stability of $AmVO_3$ and $AmVO_4$ under self-irradiation and heat treatment in an inert and oxidizing atmosphere was tested and discussed relative to other americium-containing compounds.

2. EXPERIMENTAL SECTION

Caution: ^{241}Am is a highly radioactive isotope ($t_{1/2}$ = 432.8 years, specific activity of 126.8 GBq/g). All work presented in this paper were carried out in glove boxes in radiological laboratories licensed for handling actinides. When appropriate, shielding and remote handling tools were used to protect the workers in these experiments.

2.1. Sample Preparation. *2.1.1. AmVO3.* Stoichiometric amounts of $^{241}AmO_2$ (158 mg of aged material containing about 7% ^{237}Np as the decay product and 2% ^{239}Pu) and V_2O_5 (48 mg, Merck, 99.95%) were mixed in an agate mortar and pressed into a pellet. The thermal treatment was performed for 10 h at 1250 °C under Ar/H_2 (5%) with heating and cooling ramps of 200 °C/h.

2.1.2. AmVO4. A chip of 78 mg of the previous $AmVO_3$ pellet was oxidized for 2 h up to 1000 °C under oxygen by using a Netzsch STA
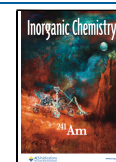
449C thermogravimetric analysis instrument. Oxidation started at about 400 °C with a maximum oxidation rate at 450 °C, as discussed in the Materials Characterization section. This synthesis was done independently from the thermogravimetric analysis described below during in which higher temperatures were reached.

2.2. Thermogravimetric Analysis. The thermal behaviors of $AmVO_3$ and $AmVO_4$ were assessed under an argon/hydrogen and oxygen atmosphere, respectively (to preserve the oxidation state of the respective compounds) using a Netzsch STA 449C thermogravimetric analysis instrument. The temperature was controlled by a Pt-PtRh (10%) thermocouple. The measurements were conducted on pellet fragments (11−78 mg) up to 1500 °C in alumina crucibles, and the applied heating and cooling rates were 10 °C/min.

2.3. XRD. Room temperature XRD analyses were performed on about 10 mg of powdered material loaded in a bicomponent epoxy resin using a Bruker D8 Advance diffractometer (Cu Kα radiation, 40 kV, 40 mA) mounted in a Bragg−Brentano configuration. The diffractometer was equipped with a curved Ge(1,1,1) Kα_1 monochromator, a ceramic copper tube, and a LinxEye position sensitive detector. The XRD patterns were recorded using a step size of 0.01° across the $10° \leq 2\theta \leq 120°$ angular range. Structural analysis was performed by the Rietveld method using the Jana2006 software.[8]

Since all the crystallographic parameters could not be independently refined, some structural constrains were applied. For the atomic displacement parameter, isotropic displacement parameters U_{iso} were used, and the following equation has been considered:[9]

$$U_{iso}[O] = 2 \times U_{iso}[Am] = 2 \times U_{iso}[V] \qquad (1)$$

The V−O distances were constrained to 2 Å for the perovskite structure $AmVO_3$[10] and to 1.71 Å for the zircon structure $AmVO_4$.[11]

2.4. Raman Spectroscopy. Raman spectroscopy measurements were performed on fragment of pellets (2−3 mg) at room temperature and ambient pressure on a polycrystalline specimen using a Horiba Jobin-Yvon T64000 spectrometer. For technical reasons, two lasers at different wavelengths were used; a 647 nm Kr+ laser and a 660 nm solid state laser excitation source. A 50× long focal objective was used to irradiate the sample and collect the back-scattered light. Great care was taken to avoid sample damage or laser-induced heating. Measurements were performed with few tenths of a milliwatt incident power.

2.5. Scanning Electron Microscopy. Images of the samples (fragment of pellets of 1−2 mg) were obtained in a Philips/FEI XL40 SEM operated at 25 kV, equipped with a SAMx energy-dispersive X-ray analysis system (EDX). This microscope (high-voltage unit, column, chamber, and turbomolecular pump) was placed inside a glovebox, while the components that are not getting in contact with the active materials (primary vacuum system, the water-cooling circuit, and the acquisition electronic) were outside.[12]

2.6. XANES and HR-XANES. For $AmVO_3$ and $AmVO_4$ compounds, the Am M_5 HR-XANES spectroscopy technique was performed at the ACT station of the beamline for catalysis and actinide research (hereafter CAT-ACT beamline) of the KIT Light Source, Karlsruhe, Germany.[13] Spectra acquisitions were done utilizing a Johann type X-ray emission spectrometer. The incident beam was monochromatized by a Si(111) double-crystal mono-chromator (DCM), focused to 500 × 500 μm, and subsequently narrowed down by slits onto the sample to a spot size of about 200 × 200 μm. The X-ray emission spectrometer consists of four Si(220) crystals with a 1 m bending radius and a single diode VITUS silicon drift detector (Ketek, Germany), which together with the sample were arranged in a Rowland circle geometry.[13] AmO_2 reference sample was used to calibrate Am M_5 HR-XANES spectra. The main absorption maximum was set to 3890 eV for AmO_2.[14] The maxima of the WLs are located at $AmCl_6^{3-}$ (3888.4 eV), $AmFe_2$ (3887.5 eV) reported elsewhere.[15,16] Both Am M_5 edge data cited above were measured in conventional fluorescence mode and were similar to $AmVO_3$ and $AmVO_4$ (3888.5 eV) recorded in this work. The slight divergence of the absorption maximum of AmO_2 in the current work (3890 eV) from the data reported by Epifano *et al.*[17] (about 3891.5 eV) is a result of different experimental energy resolutions (for details cf.

Discussion in the Supporting Information and Figure S5). The multi-position sample cell (containing <1 mg powdered material embedded in bicomponent glue) was placed into a double containment, where the inner compartment was sealed by 8 μm and the outer compartment by 13 μm Kapton foil. The HR-XANES spectra were measured with a step size of 0.1 eV from −10 to +25 eV from the white line (WL) of the respective edge and 0.5 eV in all other parts of the spectra. At least two spectra were averaged for each sample. The sample, crystals, and detector were enclosed in a box filled with helium to minimize intensity losses due to scattering and absorption of photons in air. Constant helium flow was maintained to keep the oxygen level below 0.1%.

Additionally, Am L_3 edge and V K-edge XANES measurements were performed at the INE-Beamline[18] of the KIT Light Source, Karlsruhe, Germany. The radiation protection measures were kept identical to those used at the ACT station.[19] Two Ge(422) and two Si(111) crystals were mounted in the double-crystal monochromator (DCM) for Am L_3 and V K edge measurements, respectively. The beam was focused on a ~0.5 mm × 0.5 mm spot on the sample. Zr or V metal foils were used for energy calibration for the Am L_3 edge or V K edge XANES, respectively. V_2O_3 (Sigma-Aldrich, 99.99%) and V_2O_5 (Merck, 99.95%) powders were mixed with cellulose and pressed into the pellets and used as references for V K edge XANES. The XANES spectra were measured in fluorescence mode with step sizes of 0.25 and 0.8 eV from −10 to +25 eV from the white line (WL) of the respective edges for the V K edge and Am L_3 edge and 4 eV steps in the post-edge area of the spectra. At least two spectra were averaged for each sample. Measurements were performed in air, and no radiation damage was observed during the measurements.

2.7. α Self-Irradiation. Due to the high alpha activity of americium, the doses accumulated by the $AmVO_3$ and $AmVO_4$ at the time of different measurements must be considered. Daily doses of about 7.8×10^{15} and 7.4×10^{15} α/g were built up for $AmVO_3$ and $AmVO_4$, respectively. Only TGA and XRD techniques could be applied on freshly prepared material. The calculated doses of the materials at the time of the different measurements are summarized in Table 1. Between measurements, the samples were stored under the atmosphere of the glovebox where the samples were produced (nitrogen with up to 10,000 ppm oxygen).

Table 1. α Dose Accumulated in $AmVO_3$ and $AmVO_4$ at the Time of the Different Measurements, in α Decay Events per Gram of Material

	$AmVO_3$		$AmVO_4$	
	sample age, days	cumulated dose, α/g	sample age, days	cumulated dose, α/g
XRD	1.6	1.2×10^{16}	2.7	2.1×10^{16}
	132	1.0×10^{18}	131	1.0×10^{18}
	212	1.6×10^{18}	211	1.6×10^{18}
TGA	3.4	2.7×10^{16}	2.5	1.9×10^{16}
Raman	451	3.5×10^{18}	450	3.5×10^{18}
	890	6.8×10^{18}	890	6.8×10^{18}
SEM	660	5.1×10^{18}	659	5.1×10^{18}
Am L_3 edge XANES, Am M_5 edge HR-XANES	603	4.7×10^{18}	607	4.7×10^{18}
V XANES	726	5.6×10^{18}	727	5.6×10^{18}

3. RESULTS AND DISCUSSION

3.1. Materials Characterization: Fresh Material. During the synthesis of $AmVO_4$ by oxidation of an $AmVO_3$ specimen, the DTA measurement (Figure S1) performed in oxygen indicated a single exothermic event reaching a maximum energy release at 450 °C with an associated weight gain of 4.5
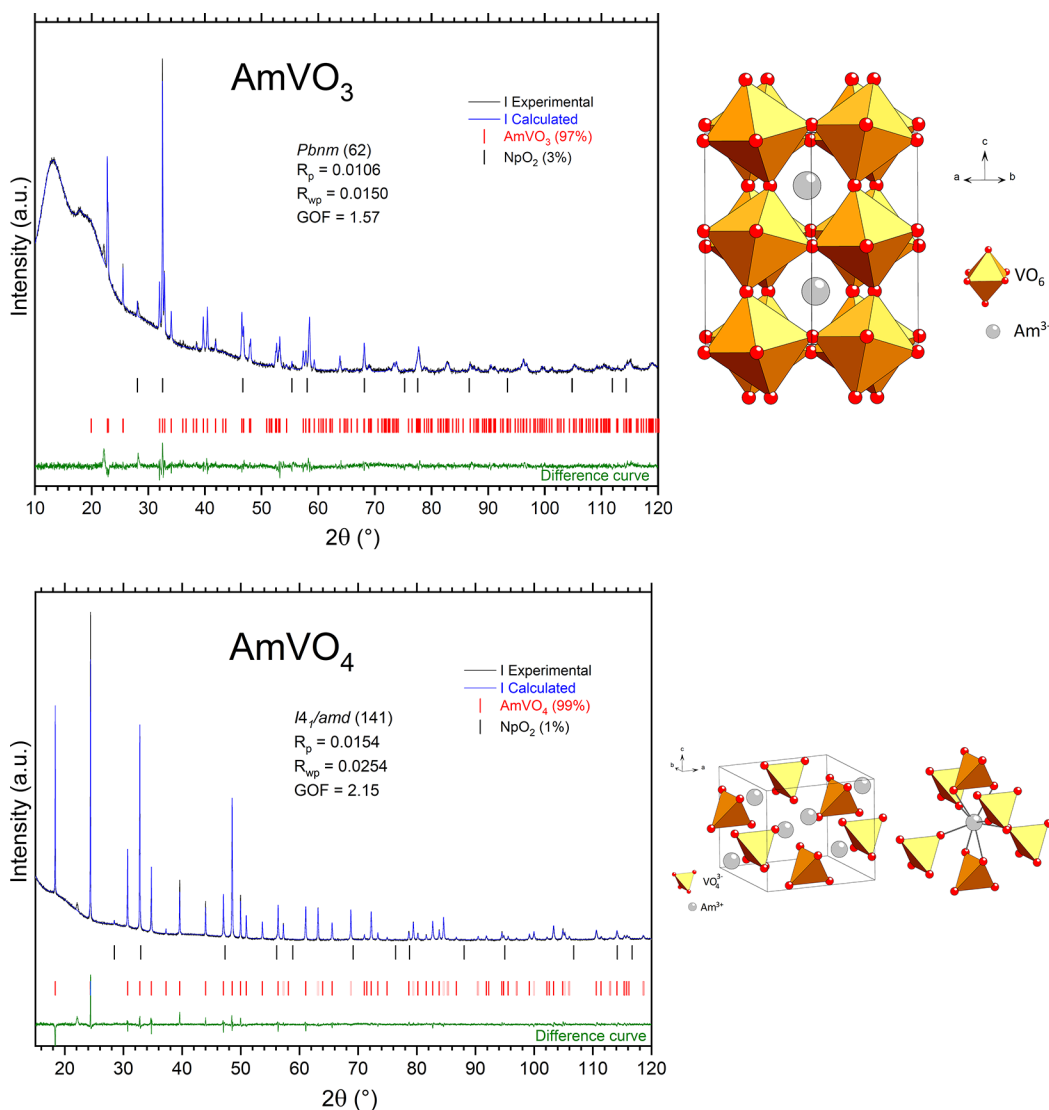
Figure 1. XRD patterns, Rietveld refinement, and crystal structure of $AmVO_3$ and $AmVO_4$.

wt %, which was attributed to the oxidation to the $AmVO_4$ form (expected gain of 4.7 wt %).

Americium vanadate $AmVO_3$ crystalizes in the perovskite *Pbnm* structure after sintering under an Ar/H_2 atmosphere; meanwhile, after thermal treatment in oxidative conditions, the material converts into $AmVO_4$ showing a zircon-like $I4_1/amd$ structure (Figure 1 and Table 2). Residual NpO_2 can be detected in quantifiable amounts, which indicates that this daughter element of ^{241}Am does not fully integrate the two vanadate compounds and segregates (at least partially) into an oxide phase. The Np L_3 edge XANES data are shown in Figure S4, supporting the above statement.

The crystal structures suggest that americium stays in the oxidation state III in the materials whatever the redox condition, while vanadium can have the oxidation state III or V, which results in ABO_3 perovskite or ABO_4 zircon structures, respectively. One can notice that during the oxidation process, the density of the material strongly decreases from 9.565 g/cm^3 for the close-packed $AmVO_3$ to 6.914 g/cm^3 for the oxyanionic $AmVO_4$, which indicates a volume increase of 45% during oxidation. The formation of a zircon-like structure for $AmVO_4$ is in accordance with the works of Keller *et al.*[6,7] or of

Goubard *et al.*[20] showing slightly lower but similar lattice parameters (Table 2).

TGA analyses, under air and argon/hydrogen for $AmVO_4$ and $AmVO_3$, respectively, revealed no significant weight loss for both materials, indicating a good thermal stability of the compounds at high temperature. However, XRD analysis of $AmVO_3$ after TGA measurement showed the presence of a new unidentified phase, $AmVO_3$ remaining as the main compound, suggesting the beginning of a degradation of the material at this temperature. In contrast, XRD measurement of $AmVO_4$ after TGA showed that the material remains fully unchanged, indicating an excellent thermal stability of this material under oxidative conditions.

The evolution of the unit-cell parameters/volumes of the MVO_3 and MVO_4 compounds (Figure 2) confirms that the Am-vanadates belong to the corresponding crystallographic families. Only the perovskite phases crystalizing in the orthorhombic *Pbnm* space group are considered in the MVO_3 part of Figure 2. The atomic coordinates and displacement parameters for $AmVO_3$ and $AmVO_4$ compounds are presented in Table 3.

3.2. Materials Characterization: α Self-Irradiated Material. Due to the impact of the COVID-19 pandemic,

Table 2. Unit Cell Parameters and Results of the Rietveld Refinement for AmVO₃ and AmVO₄[a]

formula unit	AmVO₃	AmVO₄	AmVO₄ (Keller et al.[7])	AmVO₄ (Goubard et al.[20])
space group	Pbnm	I4₁/amd	I4₁/amd	I4₁/amd
space group number	62	141	141	141
a, Å	5.4445(3)	7.2938(2)	7.31(1)	7.311(2)
b, Å	5.5914(3)	7.2938(2)	7.31(1)	7.311(2)
c, Å	7.7556(4)	6.4284(2)	6.42(1)	6.422(2)
α, °	90	90	90	90
β, °	90	90	90	90
γ, °	90	90	90	90
V, Å³	236.10(2)	341.992(10)	343	343.26
Z	4	4	4	4
M, g/mol	340.00	356.00	356.00	356.00
crystallographic density, g/cm³	9.565	6.9142	6.89	6.89
GOF	1.57	2.15		
R_p	0.0106	0.0154		
R_{wp}	0.0150	0.0254		
R_{exp}	0.0068	0.0072		

[a]$R_p = \Sigma(i)[|yi(obs) - yi(calc)|]/\Sigma(i)[yi(obs)]$; $R_{wp} = \{\Sigma(i)-[wi(yi(obs) - yi(calc))^2]/\Sigma(i)[wi \times yi(obs)^2]\}^{1/2}$; $GOF = R_p/R_{exp}$; $R_{exp} = \{\Sigma(i)[wi \times yi(obs)^2]/(n-p)\}^{1/2}$.

SEM, XANES, and Raman characterization could only be performed about 1−2 years after synthesis. Due to the high alpha activity of ^{241}Am, the effect of self-irradiation must be considered in this condition, the main effect being amorphization of the crystal structure. The amorphization of the two vanadates was followed through XRD analyses, confirming that SEM, XANES, and Raman were performed on amorphous material. However, the results further described below seem to show only a limited impact of this amorphization on the microstructure (SEM) and electronic structure (XANES) of the two vanadates, while Raman spectroscopy showed limited impact of self-irradiation for AmVO₄ and a chemical transformation due to Raman laser heating for AmVO₃.

The XRD results reveal that the volume of the close-packed AmVO₃ perovskite structure increases by about 4.2% after a

dose of 1.03×10^{18} α/g, while that of the oxyanionic AmVO₄ zircon structure shows a contraction of about 1.8% after a similar dose (Table 4). Therefore, the increased lattice disorder under α self-irradiation in this low-density structure results in a more compact arrangement. One can clearly see the swelling in AmVO₃ and the contraction in AmVO₄ in Figure 3, with a shift of the diffraction peaks into lower and higher 2Θ values, respectively. After a dose of about 1.65×10^{18} α/g (7 months), the main diffraction peak of AmVO₃ is still visible, which indicates that the amorphization process is well advanced but not completed, while at that dose, the amorphization of AmVO₄ seems fully completed.

The SE micrographs presented in Figure 4 were recorded about 2 years after the synthesis. Even if the specimens had a relatively high level of self-irradiation at the time of the measurements, it can be observed that the microstructures are typical for solid state reactions, confirming the self-homogenization of the reaction mixture during heat treatment.

To assess the oxidation state of both americium and vanadium in the AmVO₃ and AmVO₄, XANES spectroscopy characterization was performed. Am M₅ edge HR-XANES, Am L₃ edge XANES, and V K edge XANES spectra were collected. The HR-XANES data at the Am M₅ edge reveals that Am atoms have an Am^{III} oxidation state for both AmVO₃ and AmVO₄ compounds. The energy position of the main absorption resonance (white line, WL) maximum in the AmVO₃ and AmVO₄ spectra (Figure 5, blue and red solid lines) is located at about 3888.5 eV that is characteristic of the main absorption intensity of Am^{III}, consistent with previously reported data.[14,15] Note that a very limited number of Am M₅ data are published to date. To be able to compare to published spectroscopic data on compounds containing Am^{III}, Am L₃ edge XANES experiments were also performed prior to collecting the V K-edge data. The AmVO₃, AmVO₄, and AmO₂ XANES spectra were obtained following background subtraction by fitting a linear polynomial to the pre-edge region of the absorption spectrum and normalized at the maximum (WL) intensity for Am M₅ (Figure 5) and at the high energy range for Am L₃ and V K edge data (Figures 6 and 7). The maxima of the WLs located at Am^{III}VO₃ (18,521 eV eV), Am^{III}VO₄ (18,521 eV), and Am^{IV}O₂ (18,525 eV) are
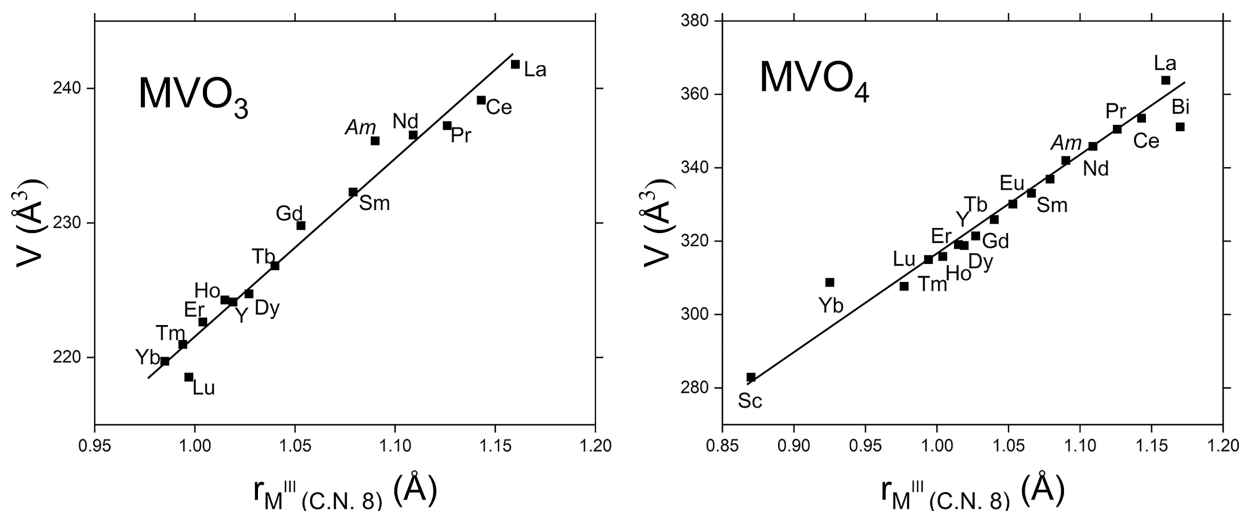

Figure 2. Evolution of the unit-cell volumes of MVO₃ and MVO₄ compounds as a function of the cationic radii. The unit-cell volume values are taken from the Inorganic Crystal Structure Database (https://icsd.fiz-karlsruhe.de) and the ionic radii from Shannon.[21]

Table 3. Atomic Coordinates and Displacement Parameters for $AmVO_3$ and $AmVO_4$ Compounds

element	label	oxidation state	SOF	Wyckoff position	x	y	z	U_{iso}, Å²
				$AmVO_3$ (*Pbnm*, perovskite)				
Am	Am1	+3	1	4c	0.9888(15)	0.0507(5)	1/4	0.004(1)
V	V1	+3	1	4b	1/2	0	0	0.004(1)
O	O1	−2	1	4c	0.397(8)	−0.010(9)	1/4	0.008(2)
O	O2	−2	1	8d	0.745(12)	0.263(11)	0.037(6)	0.008(2)
				$AmVO_4$ ($I4_1/amd$, zircon)				
Am	Am1	+3	1	4a	0	3/4	1/8	0.0074(6)
V	V1	+5	1	4b	0	1/4	3/8	0.0074(6)
O	O1	−2	1	16h	0	0.4377(11)	0.2156(17)	0.0148(12)

Table 4. Lattice Parameter Variation of $AmVO_3$ and $AmVO_4$ under Self-Irradiation

a, Å	b, Å	c, Å	V, Å³	volume variation, %	dose (α/g)	dpa[a]
			$AmVO_3$ (*Pbnm*, perovskite)			
5.444	5.590	7.755	235.982		0.01×10^{18}	0.0016
5.513	5.661	7.882	245.994	4.2	1.03×10^{18}	0.158
			$AmVO_4$ ($I4_1/amd$, zircon)			
7.294	7.294	6.428	341.952		0.02×10^{18}	0.0027
7.243	7.243	6.405	335.964	−1.8	1.02×10^{18}	0.134

[a]Estimated from the SRIM2013 simulation of displacements produced by an ^{241}Am alpha-decay (*i.e.*, an alpha-particle of 5.486 MeV and a ^{237}Np recoil nucleus of 92 keV) in $AmVO_3$ and $AmVO_4$ yielding dose multiplication factors, d, from dose to displacement per atom of 1700 and 1800, respectively.
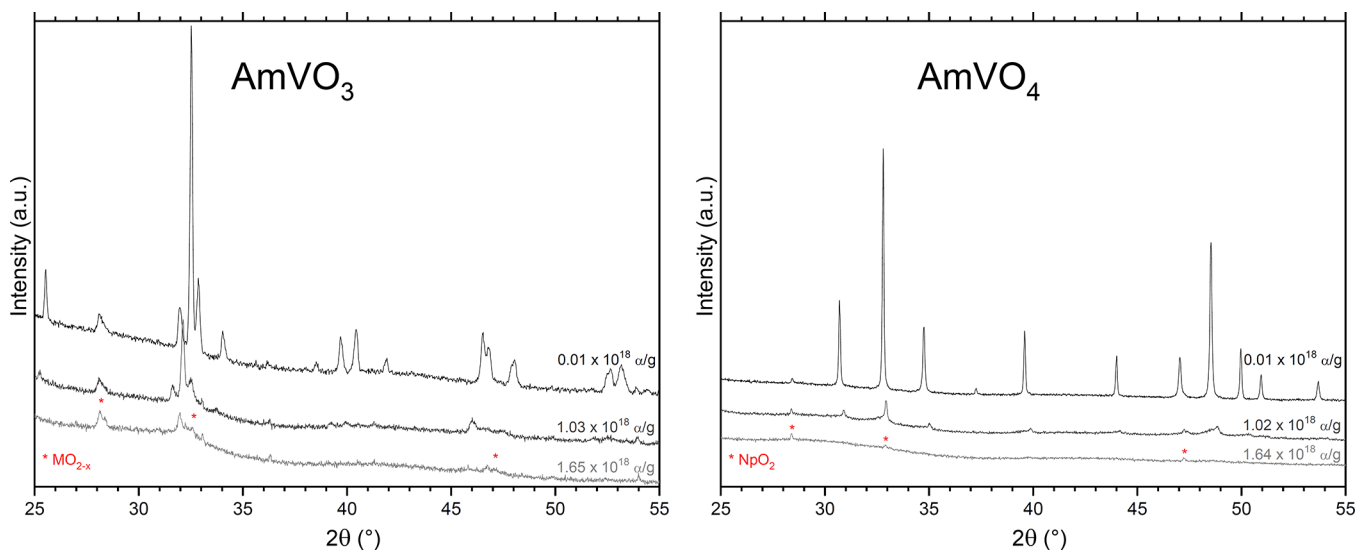
Figure 3. Evolution of the XRD pattern of $AmVO_3$ and $AmVO_4$ over time showing the progressive amorphization of the material.

similar to $Am^{III}_2O_3$ and $Am^{IV}O_2$ reported elsewhere.[22] The difference in the tail feature around 18,533 eV as well as smearing of the shape-resonance located at about 18,556 eV for $AmVO_3$ as compared to $AmVO_4$ suggests a different level of amorphization. Therefore, even though at this level of self-irradiation, both $AmVO_3$ and $AmVO_4$ are lacking a long-range order as observed by XRD, the degree of amorphization is somewhat different as revealed by Raman data (see below) and suggests that amorphization affects less the local structure in $AmVO_4$ as compared to $AmVO_3$.

To directly compare the electronic structure of vanadium, the background-subtracted and normalized V K-edge XANES spectra for $AmVO_3$ and $AmVO_4$ (blue and red solid lines, respectively) as well as reference V_2O_3 and V_2O_5 compounds (orange dotted and black dashed lines, respectively) are shown in Figure 7. As expected, for $AmVO_3$, vanadium has a V^{III}

oxidation state since all spectral features (A−D) match the spectral features of the V_2O_3 reference spectrum. The reduced intensity of the pre-edge feature A in $AmVO_3$ compared to V_2O_3 may indicate changes in the electronic structure of vanadium as a result of $AmVO_3$ amorphization due to self-irradiation effects as well as the influence of Am-presence in the resulting $AmVO_3$ after reaction of AmO_2 and V_2O_5 at 1250 °C, which differs from the pure V_2O_5 structure. The V K-edge XANES spectrum of $AmVO_4$ exhibits a strong pre-edge feature (A) characteristic to V^V that is well known to be due to a formally forbidden (very weak) 1s → 3d electronic transition, which is dipole-allowed when the local O_h symmetry is distorted.[23−25] Features B and B′ seem to be smeared out for $AmVO_4$, indicating a change of the VO_5 square-pyramidal polyhedral configuration in V_2O_5 to tetrahedral in $AmVO_4$. The findings are consistent with previously reported data by
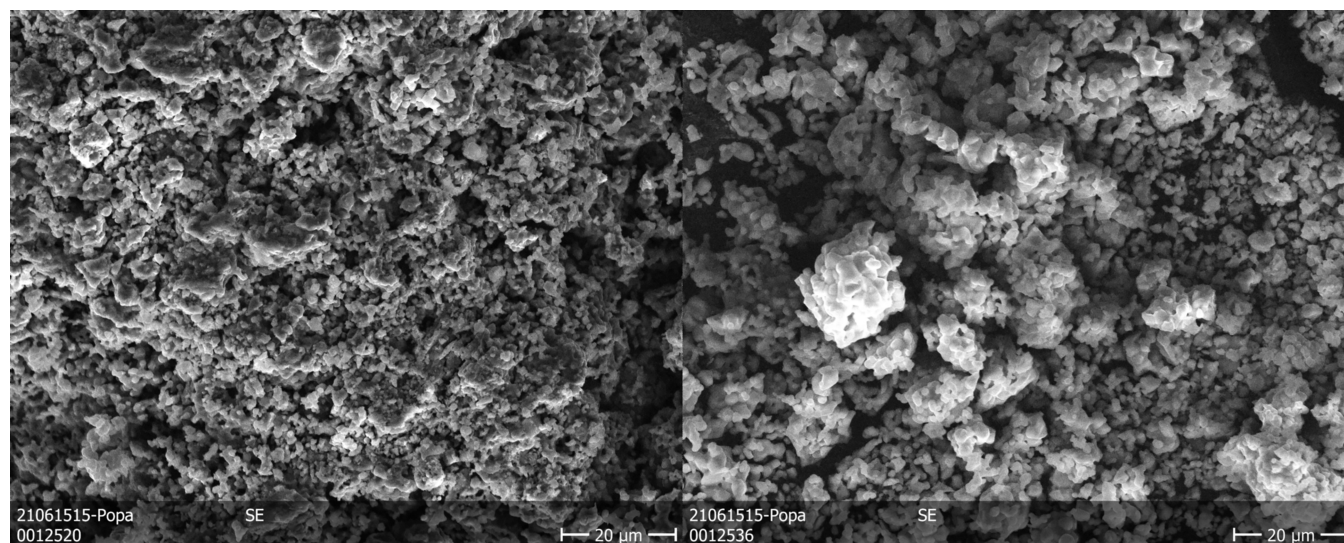
Figure 4. SE images of the microstructure of AmVO$_3$ (left) and AmVO$_4$ (right) recorded at 660 days after synthesis (5.1×10^{18} α decay events/g).
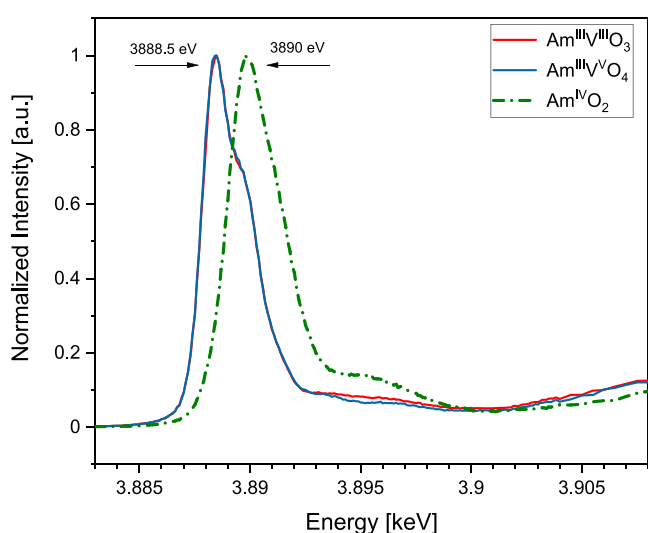

Figure 5. HR-XANES spectra acquired at the Am M$_5$ edge for AmO$_2$ (green, dash-dotted), AmVO$_3$ (red, solid, 4.7×10^{18} α/g), and AmVO$_4$ (blue, solid, 4.7×10^{18} α/g) materials. The maximum of the white line position is indicated for Am^{III} and Am^{IV} compounds, recorded at 3888.5 and 3890 eV, respectively.

Figure 6. XANES spectra acquired at the Am L$_3$ edge for AmO$_2$ (green, dash-dotted), AmVO$_3$ (red, solid, 4.7×10^{18} α/g), and AmVO$_4$ (blue, solid, 4.7×10^{18} α/g) materials. The shift of the WL maximum of 4 eV is consistent with the chemical shift between Am^{III} and Am^{IV}.

Benzi *et al.*[26] for V$_2$O$_5$ and palenzonaite (natural V^V) compounds. In that study, feature C′ in the tetrahedral geometry is located at about 5510 eV, matching the position of the shape-resonance C′ observed for AmVO$_4$.

In conclusion, all the oxidation states probed through XANES and HR-XANES measurement are in perfect agreement with the expectations based on the initial crystallographic structure of the two materials. The effect of self-irradiation and amorphization has therefore no impact on their oxidation states.

The Raman spectrum of the aged AmVO$_4$ (Figure 8) suggests that the VO$_4$ tetrahedra in the zircon-like structure are intact despite the amorphization of AmVO$_4$ at this level of self-irradiation found by XRD. The five clearly identifiable internal modes of the [V−O$_4$] tetrahedron, ν_1(A$_{1g}$), ν_3(B$_{1g}$,E$_g$), ν_4 (B$_{1g}$), ν_2(A$_{1g}$), and ν_2 (B$_{2g}$), were found at very similar wavenumbers as for the lanthanide *Ln*VO$_4$ zircon compounds,[27] as shown in Table 5, though somewhat lower than
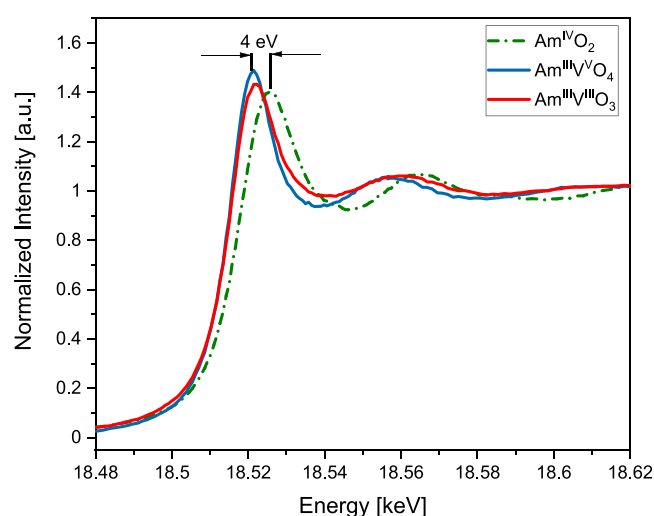
the orthovanadate of neodymium, whose ionic radius is closest to trivalent Am^{III}. The two clearly identifiable low-frequency external modes, which reflect the motion between the [V−O$_4$] tetrahedron and the Am^{III} ion, were observed, of which the lowest is the T(B$_{1g}$) and the highest is assigned to the R(E$_g$). The spectrum also shows a very weak mode at the position of one of the T(E$_g$) modes. The T(B$_{1g}$) mode is substantially lower than that found for the lanthanide *Ln*VO$_4$ compounds.[27] This can be explained by the observation by Moura *et al.*[28] that the T(B$_{1g}$) mode in the Tb(V$_{1−x}$P$_x$)O$_4$ solid solution shows a different broadening, indicating that it is related primarily to the Tb motion on the [Tb−O$_8$] sublattice. The strong shift observed here thus supports that it is due to the mass effect between the actinide and lanthanide series.

The shifts of the modes in AmVO$_4$ compared to the *Ln*VO$_4$ series are very similar to AmPO$_4$[5] and *Ln*PO$_4$.[29] However, the strong broadening of the modes after aging that was observed for AmPO$_4$ did not occur. This may be explained by
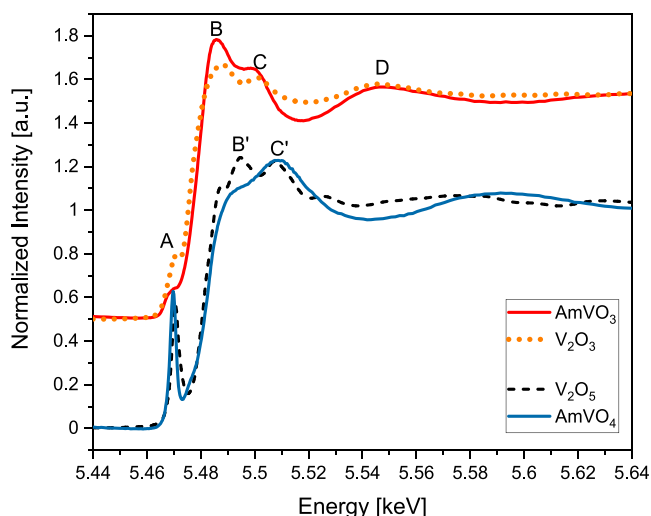
Figure 7. XANES spectra acquired at the V K edge for AmVO$_3$ (red, solid, 5.6×10^{18} α/g) and AmVO$_4$ (blue, solid, 5.6×10^{18} α/g) along with V^{III} (orange, dotted) and V^{V} (black, dashed) references.
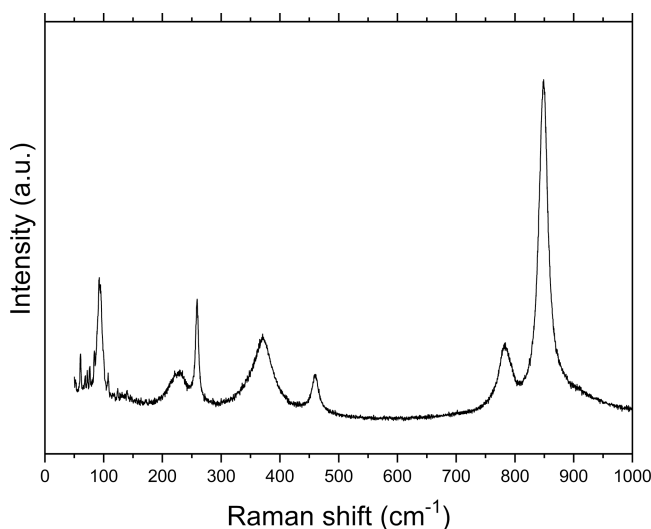

Figure 8. Room-temperature Raman spectrum of AmVO$_4$ recorded at 450 days after synthesis (3.3×10^{18} α decay events/g).

recrystallization of the amorphous AmVO$_4$ phase resulting from heating by the incident Raman laser. This would suggest relatively low critical amorphization temperatures, in line with the observations for the monazite and zircon LnPO$_4$ analogues.[29]

Surprisingly, the Raman spectrum of the aged AmVO$_3$ sample was identical to that of AmVO$_4$, suggesting that oxidation took place. We exclude that the oxidation is related to the damage build-up since it is not observed in the XRD and XANES results at similar dose. We therefore conclude that it is triggered by heating the laser during the Raman measurement.

3.3. Closer Look at the α Self-Irradiation Mechanism in AmVO$_4$. Our results for AmVO$_4$ amorphization derived from XRD analysis differ significantly from the observations in the study of Goubard et al.,[20] who studied the radiation damage build-up in AmVO$_4$ during a much longer period of 5 years (14×10^{18} α/g). They reported that the structure remained at least partially crystalline during this period and became predominantly amorphous after 5 years, which is about 10 times slower than in our work. Moreover, Goubard et al.[20]

Table 5. Raman Modes of AmVO$_4$ (in cm^{-1}) Compared to Some Lanthanide Analogues[a]

	AmVO$_4$	LaVO$_4$	CeVO$_4$	NdVO$_4$	SmVO$_4$
	this work	Cheng et al.[31]	Panchal et al.[30]	Nguyen et al.[32]	Santos et al.[27]
ν_1(A$_{1g}$)	850	859.0	864.3	871	877
ν_3(E$_g$)	785	796.7	801.3	795	816
ν_3(B$_{1g}$)	785	783.3	789.1	808	816
ν_4 (B$_{1g}$)	457	462.3	468.9	472	477
ν_2(A$_{1g}$)				381	380
ν_4 (E$_g$)	370	376.6	381.1		
ν_2 (B$_{2g}$)	255	262.9	261.9	375	
T(B$_{1g}$)					261
R(E$_g$)	225	228.7	234.1	237	240
T(E$_g$)	[140]	141.8			
T(B$_{1g}$)	95	119.7	124.4	123	123
T(E$_g$)		109.5		113	112

[a]We follow the band assignment for CeVO$_4$ by Panchal et al.[30] that was supported by density functional theory (DFT) calculations.

did not observe a volume contraction under α self-irradiation like in the present study, but a moderate lattice expansion with a volume increase to a maximum of about $\Delta V/V_0 = 1.2\%$. At a comparable dose to our study (1×10^{18} α/g), they found $\Delta V/V_0 = 0.15\%$.

The reasons for the discrepancies with the work of Goubard et al.[20] remain unclear, and one can only hypothesize the following:

- A different content of neptunium (daughter element of americium) in the initial material. Note that Goubard et al.[20] did not give details about the purity of the used Am. The exact quantity of Np that could be incorporated in AmVO$_4$ is not known, but we observed NpO$_2$ as the separate phase in this work. Moreover, uptake of Np^{IV} in the structure would require charge compensation, for example, by V^{III}, which was not observed by XANES in our work.

- The higher synthesis temperature in the current work (1000 °C vs 600 °C), which could have resulted in a more crystalline material and thus less initial disorder. As a result, a potential time span of contraction could have been absent or short in the study by Goubard et al.[20] It should be noted that their first data point at 0.7×10^{18} α/g is anomalous in their $\Delta V/V_0$ vs dose curve and indicates a minimal expansion ($\Delta V/V_0 = 0.03\%$) after approximately 90 days.

- The difference in production scale (hundreds of milligrams here versus 1 mg by Goubard et al.[20]) and more probable methods (synthesis temperature and duration) could have resulted in substantially different crystallite sizes, powder morphologies, and densities, thus potentially affecting the impact of the alpha decay through annihilation of defects, in particular via diffusion to sinks (grain boundaries).[33]

- Radiogenic helium can interact with defects (vacancies), but the effect of this will depend on the microstructure and crystallinity. The larger the grain size, the larger the helium fraction retained in the lattice, affecting the defect recombination kinetics. Similarly, the initial disorder (crystallinity) will affect the helium retention. Unfortunately, information on the microstructure of the material synthesized by Goubard et al.[20] is missing.

The first three hypotheses could explain the slight difference of the initial lattice parameters (see Table 2), but not the different kinetics. Although the damage kinetics could be affected by size and geometry of samples analyzed in the XRD instruments, the discrepancy is huge. The last two hypotheses could explain the different recombination kinetics, but remain speculative, in the absence of comparative microstructural data.

Our observations for zircon-type $AmVO_4$ are different from our results for the monazite-type $AmPO_4$.[5] The zircon structure is closely related to the monazite $LnMO_4$ structure, both made of isolated tetrahedra of V or P, connected by trivalent metal ions in eight or nine coordinations, respectively. Under the influence of temperature and/or pressure, a transition can take place.[30,31] For $AmPO_4$, a significant expansion of the unit cell was observed ($\Delta V/V_0$ = 1.8% at 0.6×10^{18} α/g), whereas the $AmVO_4$ cell contracts with irradiation time. However, the dose at which the transition to a fully amorphous phase takes place is close in both studies, slightly higher for $AmVO_4$ compared to $AmPO_4$, which is in line with the observation of Meldrum et al.[29] that the critical amorphization temperature is slightly higher for zircon-type $LnPO_4$ compounds as well.

These contrasting observations are not easy to combine. Volume contraction due to α self-irradiation is known for $Am_2Zr_2O_7$ pyrochlore[34] and was attributed to the stability of the $[Zr-O_6]$ octahedra and their rotation in response to the increase in disorder around americium. Although $Am_2Zr_2O_7$ has a close-packed pyrochlore structure, which is very different from the open oxyanionic structures of zircon and monazite, this explanation may help understand. The volume in the $LnVO_4$ series is discontinuous, with the zircon (xenotime) structure (eight-coordinated M^{III}) being larger than the monazite (nine coordination),[35] similar to the $LnPO_4$ series.[36] So, in case the radiation damage in zircon-type $AmVO_4$ affects predominantly the americium coordination sphere leading to a higher coordination with a concomitant rotation of the $[V-O_4]$ tetrahedra, the volume will decrease, as we observed here. In $AmPO_4$, the Am ions are already nine-fold coordinated, resulting in prompt expansion of the lattice with increasing dose. Of course, also differences in the radiation resistance of the $[V-O_4]$ and $[P-O_4]$ tetrahedral entities may play a role.

4. CONCLUSIONS

Two americium vanadates were produced and characterized in terms of crystal structure, cation oxidation states, and chemical, thermal, and radiation stability. The XRD and XANES measurements demonstrate that americium stays in the oxidation state III in the material whatever the redox condition, while vanadium shows the oxidation state III in the perovskite-like $AmVO_3$ or V in the zircon-like $AmVO_4$.

After an accumulation of a dose of 10^{18} α/g, the close-packed $AmVO_3$ shows a volume expansion of 4.2% while the low density oxyanionic $AmVO_4$ contracts with 1.8% in volume (in contrast with other literature reports[20]). With a fast amorphization behavior, large volume variation, and inter-changeable structure as a function of the presence of the oxygen atmosphere and temperature, americium vanadates do not appear to be good candidates as Am forms for radioisotope power systems. Moreover, ^{237}Np (the decay product of ^{241}Am) tends to segregate as a fluorite fcc secondary phase, creating interfaces and inducing stress in the material. Comparing the existing data on Am-containing ceramics with fluorite,[3] pyrochlore,[34] zircon, monazite,[5] and perovskite[4] structures,

the $(Am,U)O_2$[2,3] fluorite solid solution seems currently to be the most suitable form for space applications.

◼ ASSOCIATED CONTENT

Ⓢ Supporting Information

The Supporting Information is available free of charge at https://pubs.acs.org/doi/10.1021/acs.inorgchem.3c00251.

> Thermogravimetric behavior of $AmVO_3$ and $AmVO_4$; overview of the $AmVO_3$ and $AmVO_4$ specimens measured by SEM and EDX; XRD diffraction pattern of $AmVO_3$ after TGA measurement; Np L_3 XANES spectra of the $AmVO_3$ and $AmVO_4$; discussion on the difference in the experimental energy resolution leading to an energy shift of the main maxima of the An $M_{4,5}$ edge HR-XANES spectra; discussion on the neptunium dioxide residual phase from XRD data (PDF)

Accession Codes

CCDC 2184177−2184178 contain the supplementary crystallographic data for this paper. These data can be obtained free of charge via www.ccdc.cam.ac.uk/data_request/cif, or by emailing data_request@ccdc.cam.ac.uk, or by contacting The Cambridge Crystallographic Data Centre, 12 Union Road, Cambridge CB2 1EZ, UK; fax: +44 1223 336033.

◼ AUTHOR INFORMATION

Corresponding Authors

Jean-François Vigier − *European Commission, Joint Research Centre (JRC), Karlsruhe 76125, Germany;* ⓞ orcid.org/0000-0002-3640-1098; Email: jean-francois.vigier@ec.europa.eu

Karin Popa − *European Commission, Joint Research Centre (JRC), Karlsruhe 76125, Germany;* ⓞ orcid.org/0000-0003-2759-6492; Email: karin.popa@ec.europa.eu

Authors

Thierry Wiss − *European Commission, Joint Research Centre (JRC), Karlsruhe 76125, Germany*

Natalia Palina − *Institute for Nuclear Waste Disposal (INE), Karlsruhe Institute of Technology, D-76021 Karlsruhe, Germany*

Tonya Vitova − *Institute for Nuclear Waste Disposal (INE), Karlsruhe Institute of Technology, D-76021 Karlsruhe, Germany;* ⓞ orcid.org/0000-0002-3117-7701

Jean-Yves Colle − *European Commission, Joint Research Centre (JRC), Karlsruhe 76125, Germany*

Daniel Bouëxière − *European Commission, Joint Research Centre (JRC), Karlsruhe 76125, Germany*

Daniel Freis − *European Commission, Joint Research Centre (JRC), Karlsruhe 76125, Germany*

Rudy J. M. Konings − *European Commission, Joint Research Centre (JRC), Karlsruhe 76125, Germany*

Complete contact information is available at:
https://pubs.acs.org/10.1021/acs.inorgchem.3c00251

Notes

The authors declare no competing financial interest.

■ REFERENCES

(1) Campbell, C.; Carrigan, C.; Carrott, M.; Maher, C.; McLuckie, B.; Mason, C.; Gregson, C.; Griffiths, T.; Holt, J.; Sarsfield, M.; Taylor, R.; Tinsley, T.; Stephenson, K. The separation of ^{241}Am from aged plutonium dioxide for use in radioisotope power systems. *Procedia Chem.* **2016**, *21*, 140−147.

(2) Ambrosi, R. M.; Williams, H.; Watkinson, E. J.; Barco, A.; Mesalam, R.; Crawford, T.; Bicknell, C.; Samara-Ratna, P.; Vernon, D.; Bannister, N.; Ross, D.; Sykes, J.; Perkinson, M.-C.; Burgess, C.; Stroud, C.; Gibson, S.; Godfrey, A.; Slater, R. G.; Reece, M. J.; Chen, K.; Simpson, K.; Tuley, R.; Sarsfield, M.; Tinsley, T. P.; Stephenson, K.; Freis, D.; Vigier, J.-F.; Konings, R. J. M.; Fongarland, C.; Liberssart, M.; Merrifield, J.; Kramer, D. P.; Byrne, J.; Foxcroft, B. European Radioisotope Thermoelectric Generators (RTGs) and Radioisotope Heater Units (RHUs) for space science and exploration. *Space Sci. Rev.* **2019**, *215*, 1−41.

(3) Vigier, J.-F.; Freis, D.; Pöml, P.; Prieur, D.; Lajarge, P.; Gardeur, S.; Guiot, A.; Bouëxière, D.; Konings, R. J. M. Optimization of uranium-doped americium oxide synthesis for space applications. *Inorg. Chem.* **2018**, *57*, 4317−4327.

(4) Vigier, J.-F.; Popa, K.; Martel, L.; Manara, D.; Dieste Blanco, O.; Freis, D.; Konings, R. J. M. Plutonium and americium aluminate perovskites. *Inorg. Chem.* **2019**, *58*, 9118−9126.

(5) Popa, K.; Vigier, J.-F.; Martel, L.; Manara, D.; Colle, J.-Y.; Dieste Blanco, O.; Wiss, T.; Freis, D.; Konings, R. J. M. Synthesis, characterization and stability of americium phosphate, AmPO$_4$. *Inorg. Chem.* **2020**, *59*, 6595−6602.

(6) Keller, C. *Über die Festkörperchemie der Aktiniden-Oxide*; Institut für Radiochemie, Kernforschungzentrum Karlsruhe, Gesellschaft für Kernforschung m.b.H, KFK-225, Karlsruhe, 1964.

(7) Keller, C.; Walter, K. H. Darstellung, gitterkonstanten und chemishe eigenschaften einiger ternärer oxide des plutoniums, americiums und curiums von typ M^{III}X^{V}O$_4$. *J. Inorg. Nucl. Chem.* **1965**, *27*, 1253−1260.

(8) Petříček, V.; Dušek, M.; Palatinus, L. Crystallographic computing system JANA2006: General features. *Z. Kristallogr.* **2014**, *229*, 345−352.

(9) Oka, Y.; Yao, T.; Yamamoto, N. Hydrothermal synthesis of lanthanum vanadates: Synthesis and crystal structures of zircon-type LaVO$_4$ and new compound LaV$_3$O$_9$. *J. Solid State Chem.* **2000**, *152*, 486−491.

(10) Pickardt, J.; Schendler, T.; Kolm, M. Röntgenuntersuchung von einkristallen ternärer lanthanoid-vanadium(III)-oxide *Ln*VO$_3$ (*Ln* = Gd, Dy, Er). *Z. Anorg. Allg. Chem.* **1988**, *560*, 153−157.

(11) Chakoumakos, B. C.; Abraham, M. M.; Boatner, L. A. Crystal structure refinements of zircon-type *M*VO$_4$ (*M* = Sc, Y, Ce, Pr, Nd, Tb, Ho, Er, Tm, Yb, Lu). *J. Solid State Chem.* **1994**, *109*, 197−202.

(12) Wiss, T.; Thiele, H.; Janssen, A.; Papaiannou, D.; Rondinella, V. V.; Konings, R. J. M. Recent results of microstructural characterization of irradiated light water reactor fuels using scanning and transmission electron microscopy. *JOM* **2012**, *64*, 1390−1395.

(13) Zimina, A.; Dardenne, K.; Denecke, M. A.; Doronkin, D. E.; Huttel, E.; Lichtenberg, H.; Mangold, S.; Pruessmann, T.; Rothe, J.; Spangenberg, T.; Steininger, S.; Vitova, T.; Geckeis, H.; Grunwaldt, J.-D. CAT-ACT- A new highly versatile x-ray spectroscopy beamline for catalysis and radionuclide science at the KIT synchrotron light facility KARA. *Rev. Sci. Instrum.* **2017**, *88*, No. 113113.

(14) Vigier, J.-F.; Freis, D.; Walter, O.; Dieste Blanco, O.; Bouëxière, D.; Zuleger, E.; Palina, N.; Vitova, T.; Konings, R. J. M.; Popa, K. Synthesis and characterization of homogeneous (U,Am)O$_2$ and (U,Pu,Am)O$_2$ nanopowders. *CrystEngComm* **2022**, *24*, 6338−6348.

(15) Cross, J. N.; Su, J.; Batista, E. R.; Cary, S. K.; Evans, W. J.; Cozimor, S. A.; Mocko, V.; Scott, B. L.; Stein, B. W.; Windorff, C. J.; Yang, P. Covalency in americium(III) hexachloride. *J. Am. Chem. Soc.* **2017**, *139*, 8667−8677.

(16) Magnani, N.; Caciuffo, R.; Wilhelm, F.; Colineau, E.; Eloirdi, R.; Griveau, J.-C.; Rusz, J.; Oppeneer, P. M.; Rogalev, A.; Lander, G. H. Magnetic polarization of the americium J=0 ground state in AmFe$_2$. *Phys. Rev. Lett.* **2015**, *114*, No. 097203.

(17) Epifano, E.; Naji, M.; Manara, D.; Scheinost, A. C.; Hennig, C.; Lechelle, J.; Konings, R. J. M.; Guéneau, C.; Prieur, D.; Vitova, T.; Dardenne, K.; Rothe, J.; Martin, P. M. Extreme multi-valence states in mixed actinide oxides. *Commun. Chem.* **2019**, *2*, 59.

(18) Rothe, J.; Butorin, S.; Dardenne, K.; Denecke, M. A.; Kienzler, B.; Löble, M.; Metz, V.; Seibert, A.; Steppert, M.; Vitova, T.; Walther, O.; Geckeis, H. The INE-Beamline for actinide science at ANKA. *Rev. Sci. Instrum.* **2012**, *83*, No. 043105.

(19) Schacherl, B.; Prüssmann, T.; Dardenne, K.; Hardock, K.; Krepper, V.; Rothe, J.; Vitova, T.; Geckeis, H. Implementation of cryogenic tender X-ray HR-XANES spectroscopy at the ACT station of the CAT-ACT beamline at the KIT Light Source. *J. Synchrotron Radiat.* **2022**, *29*, 80−88.

(20) Goubard, F.; Griesmar, P.; Tabuteau, A. Alpha self-irradiation effects in ternary oxides of actinides elements: The zircon-like phases Am^{III}VO$_4$ and A^{II}Np^{IV}(VO$_4$)$_2$ (A = Sr, Pb). *J. Solid State Chem.* **2005**, *178*, 1898−1902.

(21) Shannon, R. D. Revised effective ionic radii and systematic studies of interatomic distances in halides and chalcogenides. *Acta Crystallogr., Sect. A: Cryst. Phys., Diffr., Theor. Gen. Crystallogr.* **1976**, *A32*, 751−767.

(22) Nishi, T.; Nakada, M.; Suzuki, C.; Shibata, H.; Itoh, A.; Akabori, M.; Hirata, M. Local and electronic structure of Am$_2$O$_3$ and AmO$_2$ with XAFS spectroscopy. *J. Nucl. Mater.* **2010**, *401*, 138−142.

(23) Giorgetti, M.; Berrettoni, M.; Passerini, S.; Smyrl, W. H. Absorption of polarized X-rays by V$_2$O$_5$-based cathodes for lithium batteries: an application. *Electrochim. Acta* **2002**, *47*, 3163−3169.

(24) Horrocks, G. A.; Braham, E. J.; Liang, Y.; De Jesus, L. R.; Jude, J.; Velázquez, J. M.; Prendergast, D.; Banerjee, S. Vanadium K-Edge X-ray Absorption spectroscopy as a probe of the heterogeneous lithiation of V$_2$O$_5$: First-principles modelling and principal component analysis. *J. Phys. Chem. C* **2016**, *120*, 23922−23932.

(25) Deng, S.; Yuan, Z.; Tie, Z.; Wang, C.; Song, L.; Niu, Z. Electrochemically induced metal−organic-framework-derived amorphous V$_2$O$_5$ for superior rate aqueous zinc-ion batteries. *Angew. Chem., Int. Ed.* **2020**, *59*, 22002−22006.

(26) Benzi, F.; Giuli, G.; Della Longa, S.; Paris, E. Vanadium K-edge XANES in vanadium-bearing model compounds: a full multiple scattering study. *J. Synchrotron Radiat.* **2016**, *23*, 947−952.

(27) Santos, C. C.; Silva, E. N.; Ayala, A. P.; Guedes, I.; Pizani, P. S.; Loong, C. K.; Boatner, L. A. Raman investigations of rare earth orthovanadates. *J. Appl. Phys.* **2007**, *101*, No. 053511.

(28) Moura, M. R.; Ayala, A. P.; Guedes, I.; Grimsditch, M.; Loong, C. K.; Boatner, L. A. Raman scattering study of $Tb(V_{1-x}P_x)O_4$ single crystals. *J. Appl. Phys.* **2004**, *95*, 1148.

(29) Meldrum, A.; Boatner, L. A.; Ewing, R. C. Displacive radiation effects in the monazite- and zircon-structure orthophosphates. *Phys. Rev. B* **1997**, *56*, 13805.

(30) Panchal, V.; Lopez-Moreno, S.; Santamaría-Pérez, D.; Errandonea, D.; Manjón, F. J.; Rodríguez-Hernandez, P.; Muñoz, A.; Achary, S. N.; Tyagi, A. K. Zircon to monazite phase transition in $CeVO_4$. *Phys. Rev. B* **2011**, *84*, No. 024111.

(31) Cheng, X.; Guo, D.; Feng, S.; Yang, K.; Wang, Y.; Ren, Y.; Song, Y. Structure and stability of monazite- and zircon-type $LaVO_4$ under hydrostatic pressure. *Opt. Mater.* **2015**, *49*, 32−38.

(32) Nguyen, A.-D.; Murdoch, K.; Edelstein, N.; Boatner, L. A.; Abraham, M. M. Polarization dependence of phonon and electronic Raman intensities in $PrVO_4$ and $NdVO_4$. *Phys. Rev. B* **1997**, *56*, 9794.

(33) Martínez, E.; Senninger, O.; Caro, A.; Soisson, F.; Nastar, M.; Uberuaga, B. P. Role of sink density in nonequilibrium chemical redistribution in alloys. *Phys. Rev. Lett.* **2018**, *120*, No. 106101.

(34) Belin, R. C.; Martin, P. M.; Valenza, P. J.; Scheinost, A. C. Experimental insight into the radiation resistance of zirconia-based americium ceramics. *Inorg. Chem.* **2009**, *48*, 5376−5381.

(35) Baglio, J. A.; Sovers, O. J. Crystal structures of the rare-earth orthovanadates. *J. Solid State Chem.* **1971**, *3*, 458−465.

(36) Ni, Y.; Hughes, J. M.; Mariano, A. N. Crystal chemistry of the monazite and xenotime structures. *Am. Mineral.* **1995**, *80*, 21−26.

📖 Recommended by ACS